International Journal of Plasticity 139 (2021) 102944

Contents lists available at ScienceDirect

International Journal of Plasticity

journal homepage: http://www.elsevier.com/locate/ijplas

Hydrogen induced slowdown of spallation in high entropy alloy under shock loading

Zhou-Can Xie [a,b], Chen Li [a,b], Hai-Ying Wang [a,b], Chunsheng Lu [c], Lan-Hong Dai [a,b,d,*]

[a] State Key Laboratory of Nonlinear Mechanics, Institute of Mechanics, Chinese Academy of Sciences, Beijing, 100190, PR China
[b] School of Engineering Science, University of Chinese Academy of Sciences, Beijing, 101408, PR China
[c] School of Civil and Mechanical Engineering, Curtin University, Perth, WA, 6845, Australia
[d] State Key Laboratory of Explosion Science and Technology, Beijing Institute of Technology, Beijing, 100081, China

ARTICLE INFO

Keywords:
Hydrogen embrittlement
High entropy alloy
Spallation
Trans-scale model
Statistical damage mechanics

ABSTRACT

Hydrogen embrittlement is ubiquitous in metals and alloys exposed to hydrogen, which has been extensively studied over a century. In contrast to traditional alloys, mechanisms of hydrogen embrittlement under shock loading are poorly understood, especially in recently emerging multi-principle element and chemically disordered high entropy alloys (HEAs). By using a specially designed double-target technique, an unexpected phenomenon of hydrogen-retarded spallation was observed in CrMnFeCoNi HEA under plate impact loading. To reveal the underlying mechanism, a trans-scale statistical damage mechanics model was developed based on microstructural characterization and first principles calculations. The hydrogen-retarded nucleation of micro-voids is attributed to hydrogen-vacancy complexes with high migration energy, while formation of nano-twins with high resistance reduces their growth rate. These results shed light on the better understanding of hydrogen embrittlement in chemically complex HEAs.

1. Introduction

Metallic materials in a hydrogen-rich environment generally appear degradation of mechanical properties and even catastrophic failure, which is referred to as hydrogen embrittlement (Johnson, 1875). Several mechanisms have been proposed for explaining the hydrogen embrittlement of traditional alloys, including hydrogen-enhanced localized plasticity (Robertson and Birnbaum, 1986; Tabata and Birnbaum, 1983; Yuan et al., 2020), hydrogen-enhanced decohesion (Oriani, 1972; Wan et al., 2019), and hydrogen-enhanced plasticity-induced vacancy (Nagumo, 2001, 2007; Xiong et al., 2018). To scrutinize hydrogen embrittlement phenomena, a series of coupled theories were formulated that account for diffusion of hydrogen and elastic-plastic deformation of metals (Abdolvand, 2019; Castelluccio et al., 2018; Di Leo and Anand, 2013). Although its physical origin has long been controversial, it is deemed that the chemical composition and atomic-packing order play an important role in hydrogen embrittlement (Li et al., 2020b; Robertson et al., 2015).

Recently, high entropy alloys (HEAs) have drawn increasing interest as a novel class of multiple-principal element and chemically disordered alloys (Cantor et al., 2004; Yeh et al., 2004; George et al., 2019; Li et al., 2019a; Murty et al., 2019; Wang et al., 2020). As a typical five-element HEA (Cantor et al., 2004; Yeh et al., 2004), CrMnFeCoNi exhibits superior mechanical properties such as an

* Corresponding author. State Key Laboratory of Nonlinear Mechanics, Institute of Mechanics, Chinese Academy of Sciences, Beijing, 100190, PR China.
E-mail address: lhdai@lnm.imech.ac.cn (L.-H. Dai).

https://doi.org/10.1016/j.ijplas.2021.102944
Received 12 September 2020; Received in revised form 19 January 2021; Accepted 22 January 2021
Available online 2 February 2021

excellent combination of strength and ductility (Fang et al., 2019; Hasan et al., 2019; Shi et al., 2019; Gludovatz et al., 2014), shock resistance (Jiang et al., 2016; Li et al., 2018; Zhang et al., 2020), and fatigue resistance (Li et al., 2020a; Thurston et al., 2017). These remarkable properties mainly stem from their unique chemical disorder at atomic-level, where diverse elements are randomly arranged on crystallographic positions (Ding et al., 2018; Li et al., 2019b; Ming et al., 2019; Zhang et al., 2017). Furthermore, the hydrogen embrittlement sensitivity of HEAs has been investigated under quasi-static loading. Compared to traditional alloys, HEAs exhibit severe lattice distortion and nanoscale local chemical order heterogeneities, which can serve as hydrogen-trapped sites, thereby resulting in high hydrogen solubility (Pu et al., 2018; Zhao et al, 2017a,b, 2018). HEAs also exhibit excellent hydrogen resistance, particularly at low temperatures (Luo et al, 2017, 2018, 2020; Pu et al., 2018). These phenomena can be partially explained by the slow diffusion of hydrogen in HEAs due to an intrinsically rugged diffusion path (Pu et al., 2018; Zhang et al., 2017) and the decrease of stacking fault energy induced by hydrogen (Luo et al, 2017, 2018, 2020).

Generally, hydrogen embrittlement is a complex phenomenon involving a series of multi-scale and spatio-temporal coupling events such as hydrogen diffusion, dislocations and twins, as well as micro-void nucleation and growth (Barrera et al., 2018). Such an evolution process is determined by the characteristic relaxation time at the microscopic scale and an imposed time (Bai et al., 2019). Under quasi-static loading, there is sufficient time for relaxation of rate-dependent micro-events. However, these events are far from equilibrium during dynamic loading and it is necessary to consider the microstructural evolution process (Ku et al., 2020; Mayer and Mayer, 2020; Lieou et al., 2019; Rittel et al., 2008).

Spallation is a typical dynamic fracture mode with a transient tensile loading time from nano-to micro-seconds (Hopkinson, 1914). Compared with fracture governed by fracture toughness, spallation is a trans-scale process that includes the collective evolution of numerous microscopic voids or cracks (Remington et al., 2018; Kanel' et al., 2017; Bai et al., 2005; Meyers and Aimone, 1983). Curran et al. (1987) proposed a nucleation and growth model of micro-voids based on damage statistics on cross sections of a material impacted in gas gun experiments. Furthermore, the statistical evolution of micro-voids was established based on the number density conservation law in a phase space; thus, spallation of traditional alloys can be quantitatively described in the framework of continuum mechanics (Bai et al, 2000, 2019). However, when CrMnFeCoNi is applied in a hydrogen-rich environment such as deep sea and hydrogen storage, there is lack of studies on spallation of H-charged CrMnFeCoNi and the influence of hydrogen on its microscopic process.

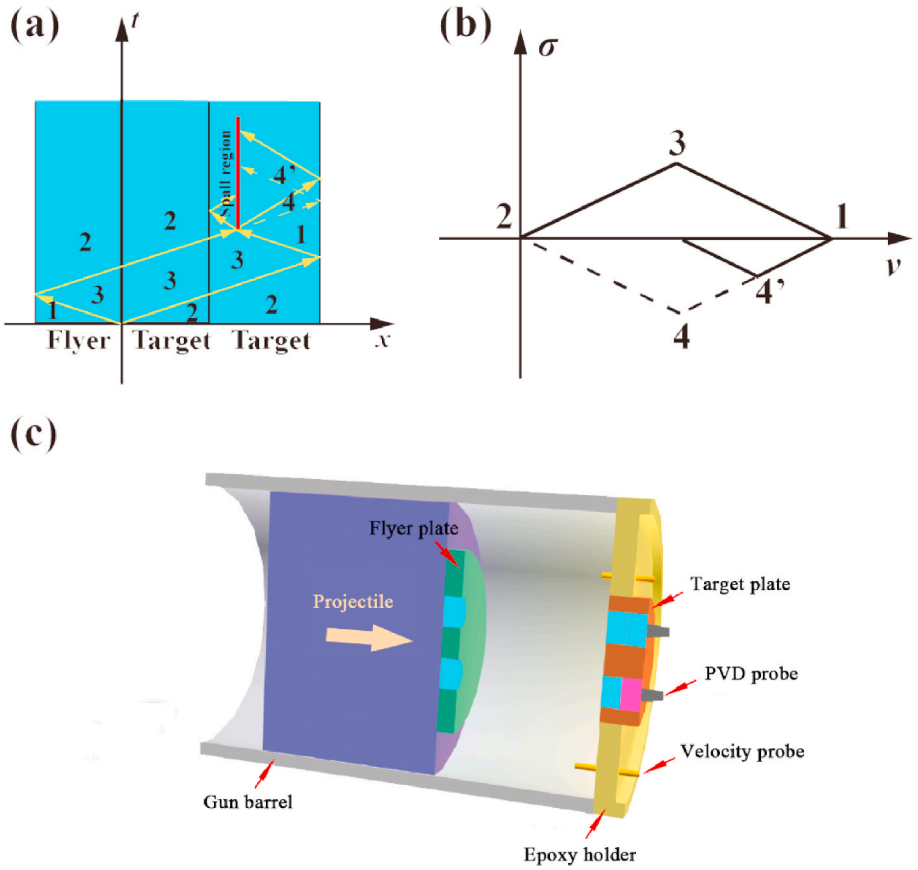

Fig. 1. (a) Time *versus* distance graph with a wave propagating in flyer and target plates under plate impact. (b) Stress *versus* particle-velocity diagram. (c) Schematic of the experimental configuration, where light blue and pink blocks represent samples without and with hydrogen, respectively. (For interpretation of the references to color in this figure legend, the reader is referred to the Web version of this article.)

In this paper, a specially designed double-target spalling experiment is performed for H-free and H-charged CrMnFeCoNi samples. The key effects of hydrogen on micro-void nucleation and growth are characterized by nanoindentation, electron backscatter diffraction, transmission electron microscopy (TEM), positron annihilation tests, and first principle calculation. Then, based on experimental observations, a trans-scale statistical model is established to consider the interaction among hydrogen, vacancy and dislocation. Finally, the process of hydrogen-retarded spallation is described quantitatively.

2. Materials and methods

An equiatomic CrMnFeCoNi ingot was produced by arc-melting pure elements in a vacuum induction furnace. To refine grains, the ingot was cold-rolled to 50% and subsequently annealed at 1150 °C for 1.5 h. The samples for spalling experiments were machined from the annealed plate and polished with fine SiC papers.

Hydrogen was introduced into the samples by using a cathodic electrochemical charging technique in 0.5 mol L^{-1} H_2SO_4 + 1 g L^{-1} CH_4N_2S (thiourea) solution with a constant current density of 100 mA cm^{-2} at 80 °C. The hydrogenation time was 48 h, and H-charged samples were immediately immersed in liquid nitrogen until tests were performed.

In electrochemically charged samples, the hydrogen distribution exhibits a concentration gradient along thickness. To determine the hydrogen content in a spalling zone, cubes of weight ~1 g were cut from a preset spallation zone of initial H-charged samples without shocking. When these cubes were melted in high-purity argon, hydrogen was released and transformed into water by a CuO catalyst. Then, the hydrogen content in water can be measured with an infrared detector.

To study the interaction between hydrogen and vacancy, positron annihilation lifetime tests were carried out. The positron source (^{22}Na) was sandwiched between two identical samples, and positrons were emitted with a broad energy distribution from 0 to 545 keV based on β-decay. Then, positrons were implanted in the samples from surface to bulk and further annihilated with an electron into two 511 keV photons. The lifetime was measured as the time lag between positron emission and annihilation. When positron was trapped in a defect, a lower density of conducting electrons resulted in a longer characteristic attenuation time. Therefore, the type and number of defects can be distinguished from their lifetime spectra. The total number of lifetime spectra was 2 million in order to ensure the statistical property, and the time resolution of a spectrometer was 210 ps. The lifetime spectra were analyzed by the LT-9.0 program (Kansy, 1996).

Nanoindentation was performed on cross sections of two H-charged samples, and hardness was measured five times at a given depth using the Agilent Nano Indenter G200 with a three-sided pyramidal indenter. The maximum indentation depth was 1.0 μm under a constant indentation strain rate of 0.05 s^{-1}. Hardness was calculated by using the continuous stiffness measurement technique (Oliver and Pharr, 1992).

To investigate the influence of hydrogen on spallation of CrMnFeCoNi, plate impact experiments were performed with a 101 mm single-stage light gas gun. As illustrated in Fig. 1(a), the abscissa represents the distance in target and flyer plates from impact surface, while the ordinate indicates the time after impact. The number is the corresponding state in Fig. 1(b), and arrows are the directions of wave propagation. The stress versus particle-velocity diagram details the locus of all normal stress and particle-velocity states that are attained during spallation. Upon impact, longitudinal compressive stress waves are generated in both the target and flyer plates. When the shock front reaches free-surface, the free surface velocity undergoes a jump from zero up to the impact velocity (State 1). Then, the interaction between the longitudinal release waves from free surfaces of flyer and target plates result in a tensile state at a pre-determined location within a rear HEA specimen. If spall strength is larger than an applied tensile stress, the state at the right of the red line transforms from State 1 to State 4. However, if a tensile stress is more than the spall strength, spallation occurs and the stress is in State 4'.

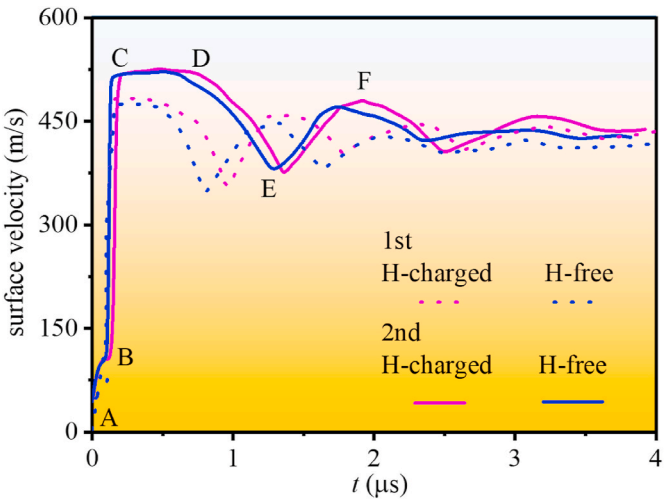

Fig. 2. Particle-velocity profiles on free surface *versus* time in experiments.

According to interactions between shock waves, spallation was designed near the charged surface to acquire a significant effect of hydrogen. To obtain samples with and without hydrogen under the same loading condition, we prepared a pair of small flyer plates, front and rear targets (an H-free and an H-charged rear targets), with corresponding thicknesses of 3.0, 3.0 and 3.1 mm, respectively. As illustrated in Fig. 1(c), flyer plates were fitted into holes in an aluminum flyer plate that was bonded to a gas-driven projectile to obtain the same impact velocity and impact plane, and targets were placed at their corresponding positions in the target plate to ensure the same impact plane. A photonic Doppler velocimetry system (Strand et al., 2006) was adopted to measure the velocity of free surface, and a pair of coaxial electric probes were embedded in an epoxy holder to record the impact velocity. To recover the spalled samples, a steel cylinder stuffed with cotton was placed at the back of a vacuum chamber. Furthermore, the deformed microstructures on cross sections of CrMnFeCoNi samples were characterized by a combination of an optical microscopy, an electron backscatter diffraction (JEOL, JSM-7100F), and TEM (JEOL, JEM-2100F).

3. Experimental results

3.1. Free surface velocity

As shown in Fig. 2, a free surface velocity profile consists of shock compression, subsequent release, and spallation. The segment (AB) indicates an elastic precursor wave, with state (B) being the Hugoniot elastic limit. Then, a plastic wave (BC) develops into a stable shock (CD), and the arrival of a release wave leads to a velocity drop (DE). Finally, the increase of an ensuing velocity (EF) is induced by a compression wave that was reflected from the spalled plane in a sample.

The impact velocities in first and second experiments were 500 and 550 m s^{-1}, respectively. The spall strength σ_{sp} can be calculated by (Meyers and Aimone, 1983)

$$\sigma_{sp} = \frac{1}{1 + C_L/C_0} \rho C_L \Delta u \tag{1}$$

where ρ is the material density, C_L is the longitudinal sound velocity, C_0 is the bulk sound velocity, and $\Delta u = u_{fs,D} - u_{fs,E}$, with $u_{fs,D}$ and $u_{fs,E}$ being the velocities at positions D and E, respectively. The spall strengths of H-free and H-charged samples in the first experiment are 2.15 and 2.18 GPa, respectively, and they are 2.53 and 2.58 GPa in the second experiment. The error estimation method is given in Appendix A, and more spall experiments are shown in Appendix B.

3.2. Statistical distribution of micro-voids

The hydrogen content measured in a spallation region varies in a range of 8–38 wppm (with an average value of 21 wppm). As shown in Fig. 3, spallation in an H-charged CrMnFeCoNi sample (~400 μm from surface) involves the evolution of numerous micro-voids, implying ductile fracture. It is obvious that the area with micro-voids in H-free samples is larger than that in H-charged ones. That is, hydrogen retards the evolution of micro-voids.

Next, an image processing technique was applied to extract the size distribution of micro-voids on cross sections. As shown in Fig. 4, the cumulative number density of micro-voids can be well fitted by an exponential function, $n = n_0 e^{-\frac{a}{a_0}}$, in the case of $a < 30$ μm, where n_0 and a_0 are the cumulative number and the average size of micro-voids, respectively. In the first experiment, the cumulative number density and the size of micro-voids in H-charged CrMnFeCoNi are significantly lower, indicating that hydrogen reduces the micro-void

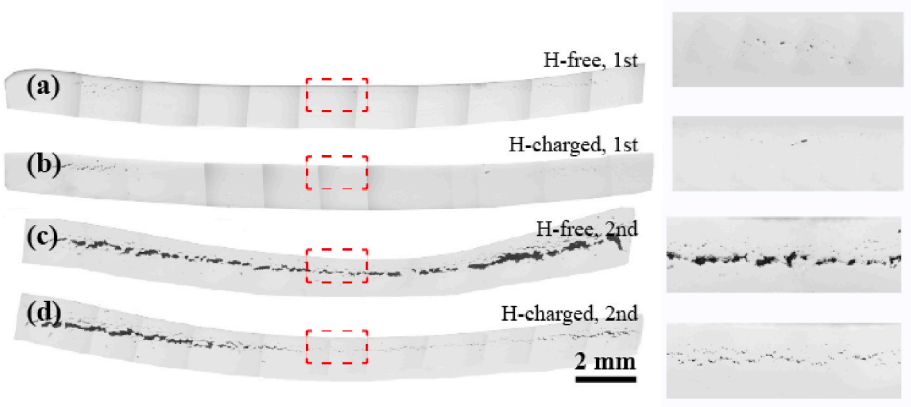

Fig. 3. Cross sections of spalled samples observed by an optical microscope, where (a) and (b) are the samples without and with hydrogen in the first experiment, and (c) and (d) are their corresponding ones in the second experiment, respectively. Images in the right column are magnified regions marked by red rectangles. (For interpretation of the references to color in this figure legend, the reader is referred to the Web version of this article.)

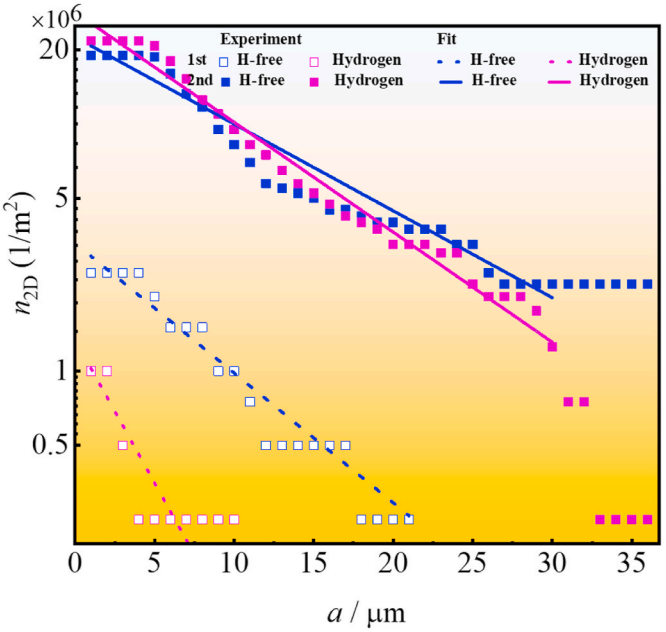

Fig. 4. Size distributions of micro-voids (>1 μm) were observed on cross sections of spalled samples.

nucleation number and growth rate. In the second experiment, the number of large micro-voids remarkably increases in H-free CrMnFeCoNi because of the coalescence of micro-voids (see Fig. 3). This is a further evidence of the hydrogen retarded coalescence of micro-voids. That is, in contrast to the traditional perception, hydrogen does not always act as a harmful impurity. It can also be utilized to retard the nucleation, growth and coalescence of micro-voids.

3.3. Material characterization

Nanoindentation was performed to determine the effect of hydrogen on local hardness of an HEA. As shown in Fig. 5, hardness decreases monotonically with increasing the distance from charged surface. That is, hydrogen enhances the local strength of HEA, which is consistent with previous studies (Luo et al., 2018; Zhang et al., 2017).

The electron backscatter diffraction mappings show that the grain size is about 50 μm. The ratios of the number of voids at grain boundaries to the total number are 100%, 100% and 77% in Fig. 6(a−c), respectively. That is, voids nucleate preferentially at grain

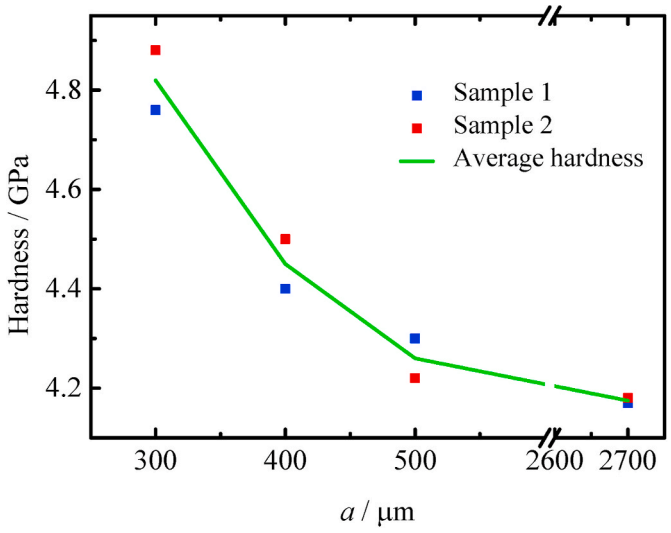

Fig. 5. Hardness as a function of distance from charged surface, where blue and red points represent two H-charged samples. (For interpretation of the references to color in this figure legend, the reader is referred to the Web version of this article.)

boundaries, except for a few interior grains (see Fig. 6). These grain boundaries provide numerous void nucleation sites due to the loose atomic arrangement and local stress concentration. Thus, the maximum number of potential nucleation sites per unit volume can be determined by the grain boundary content.

Furthermore, samples prepared for TEM characterization were cut off between two micro-voids in post-shock CrMnFeCoNi samples by using the focused ion beam technique (see Fig. 7(a)). As shown in Fig. 7(b and c), nano-twins were formed during deformation in both samples, and some secondary twins were formed in H-charged sample (Fig. 7(c)). The high-resolution image in Fig. 7(d) display a clear twin boundary in the H-free sample; however, a Lomer-Cottrell lock formed due to dislocations pinned by twin boundaries in the H-charged sample (insets in Fig. 7(e)).

The positron annihilation lifetimes were measured to study the interaction between hydrogen and vacancy. The characteristic attenuation times and intensities are listed in Table 1. Based on the assumption of two-state trapping, a quantitative relationship between the annihilation characteristic time and vacancy concentration is obtained. That is$Q = ZC_{va}$, where Q is the positron trapping rate that is related to characteristic attenuation times and intensities, $Z = 2.2\times10^{15}$ s^{-1} (Dlubek et al., 1976) is the specific trapping rate, and C_{va} is the vacancy concentration. It is shown that the initial vacancy concentration is higher in the H-charged sample (see Table 1).

4. First principles calculations and results

The micro-void nucleation rate is related to generation and migration of vacancies, except for the initial vacancy concentration. The diffusion coefficient is defined as $D_i = D_{i0}\exp(-E_{im}/kT)$, where D_{i0} is a prepositive coefficient, E_{im} is the diffusion barrier, and subscript i represents vacancy, hydrogen or hydrogen-vacancy complex. Here, first principles calculations were performed with the projector augmented wave method based on the Vienna Ab initio Simulation Package (Kresse and Furthmüller, 1996). In calculations, the plane wave cutoff energy was 420 eV, and the convergent energy and force were 10^{-5} eV and -0.03 eV $Å^{-1}$, respectively. The collinear spin polarization (i.e., ISPIN = 2) was enabled. All HEA supercells were generated by using a special quasi-random structure method and alloy theoretic automated toolkit codes (Zunger et al., 1990). HEA supercells with 80 atoms were firstly established and fully relaxed with $4 \times 4 \times 4$ K-points gird. According to Xie et al. (2021), the average value of diffusion barrier of hydrogen is 0.63 eV.

The initial vacancy and hydrogen-vacancy configurations were formed by removing an atom and replacing a metallic atom with an H atom, respectively. Their corresponding post-migration configurations were created by swapping neighbor atoms with vacancy and

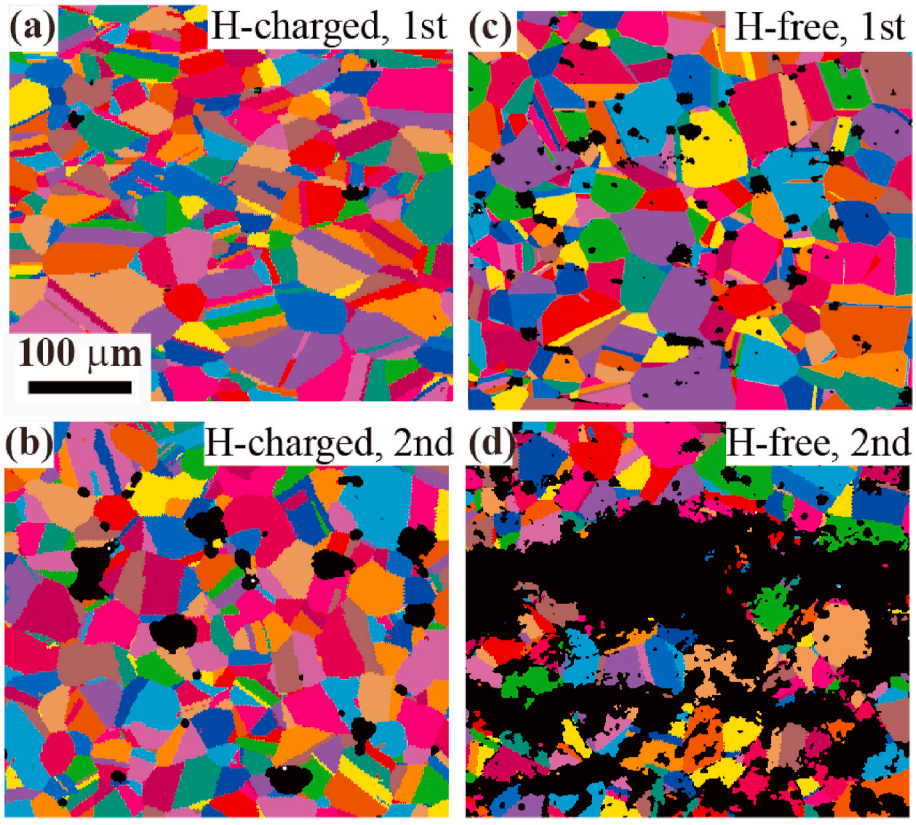

Fig. 6. Inverse pole figure maps, where (a) and (c) are samples with and without hydrogen in the first experiment, and (b) and (d) are the corresponding samples in the second experiment.

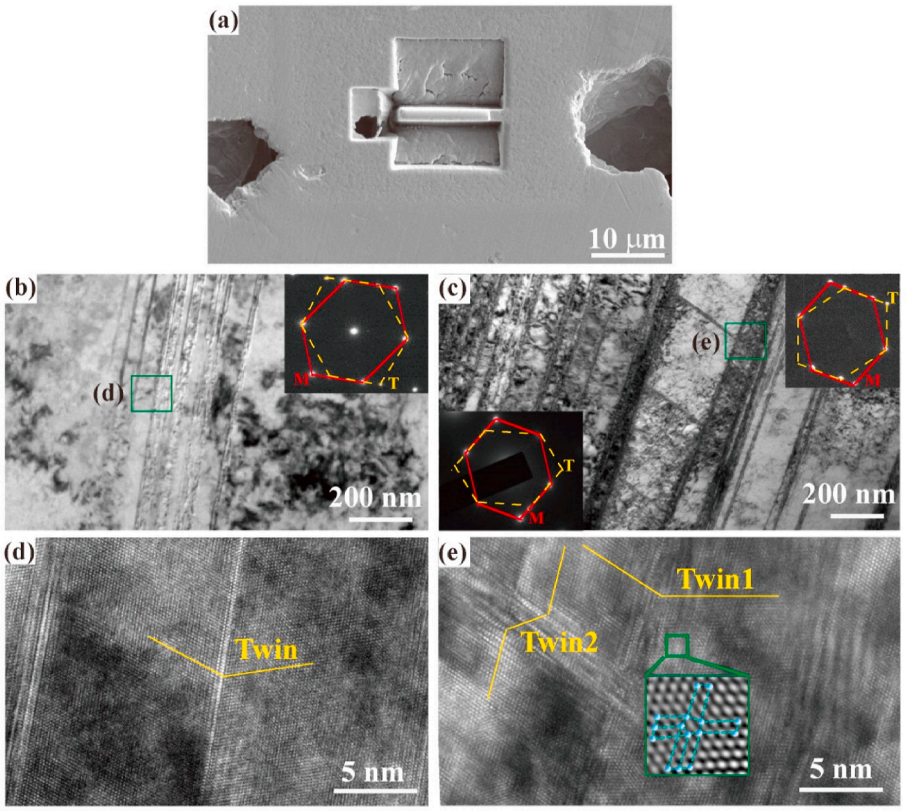

Fig. 7. (a) Scanning electron microscopy image of a region where foil was cut; (b) and (c) TEM images of H-free and H-charged CrMnFeCoNi with the selected area diffraction patterns in insets; (d) and (e) high-resolution images of H-free and H-charged CrMnFeCoNi.

Table 1
Positron lifetime spectra of samples with and without hydrogen. τ_1, τ_2 and τ_3 represent the characteristic attenuation times due to contributions of defect-free bulk, defect, and sample surface, respectively; and I_1, I_2, and I_3 represent the corresponding intensities of positron annihilation.

Sample	τ_1 (ns)	I_1 (%)	τ_2 (ns)	I_2 (%)	τ_3 (ns)	I_3 (%)	C_V (m^{-3})
H-free	0.104	82.3	0.195	17.4	1.97	0.248	1.2×10^{23}
H-charged	0.109	76.2	0.207	23.3	1.62	0.496	1.7×10^{23}

H atom, respectively. Then, initial and post-migration configurations served as the initial and final images in a climbing-image nudged elastic band method (Sheppard et al., 2012), and six intermediate structures were interpolated along a pathway and connected like a "spring band" to search the minimum energy path.

In HEAs, the spatial composition variation becomes appreciable. Electronic charge transfer of different metal atoms causes fluctuation of potential energy landscape, which diversifies diffusion barrier. As shown in Fig. 8, migration barriers depend on the species of swapping atoms and element environments, and they are adjusted by the chemical disorder of an alloy. Besides, it needs to overcome several different barriers in a diffusion path, and in such a case, the maximal barrier is chosen as the effective resistance of diffusion. The average diffusion barrier of vacancies is 0.89 eV, which is consistent with that obtained by Thomas and Srikanth (2020). The average diffusion barriers of hydrogen-vacancy complex is 1.21 eV. That is, there is a higher diffusion barrier in hydrogen-vacancy complex and vacancy is pinned by hydrogen.

According to these characterization experiments and first principles calculations, we have obtained the effects of hydrogen on the evolution of vacancies, dislocations and twins. However, there is still lack of a clear correlation between the hydrogen-induced micro-events and hydrogen-retarded macroscopic spallation, which is resorted to the following theoretical analysis.

5. A statistical micro-damage model

Spallation is a complicated dynamic failure process, which is not only involved with the imposed conditions, but also closely related to the collective evolution of numerous micro-voids. Under a hydrogen-rich environment, hydrogen affecting the spallation behavior consists of the interactions between hydrogen and several micro- and meso-scale time-dependent processes such as nucleation and

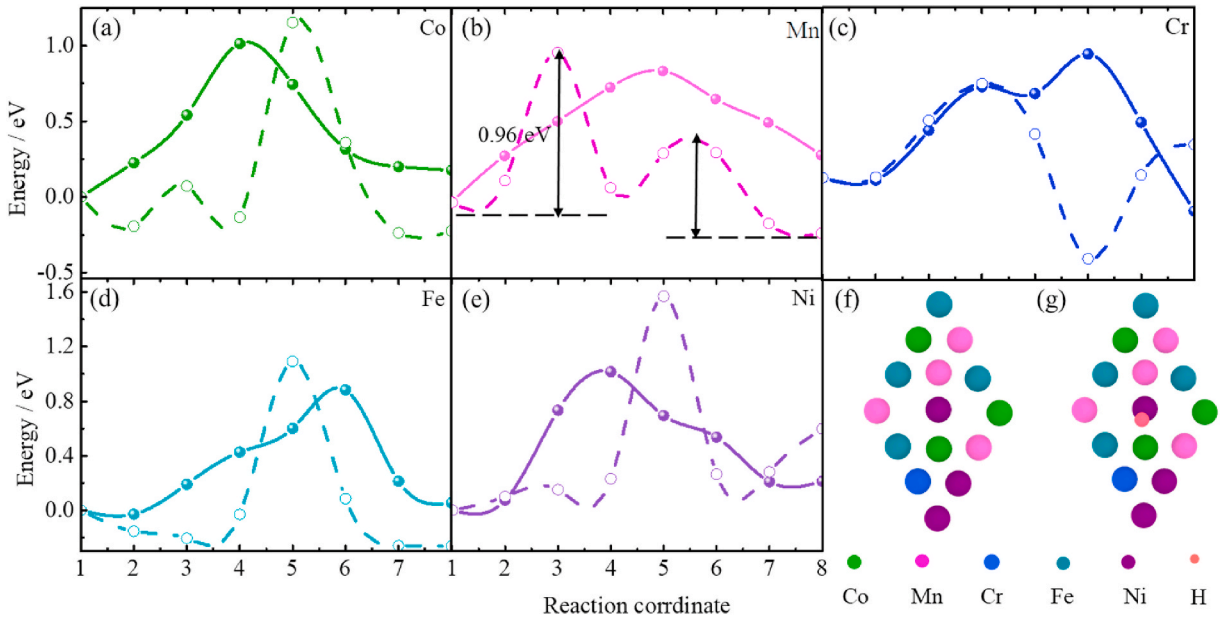

Fig. 8. (a–e) represent diffusion barriers of Co-, Mn-, Cr-, Fe- and Ni-type vacancies and hydrogen-vacancy complex, where solid and dash lines are vacancy and hydrogen-vacancy complex. (f) and (g) illustrate the saddle point configurations of Ni-type vacancy and hydrogen-vacancy complex, respectively.

evolution of microstructural defects like vacancies, twins and micro-voids, which is a typical multi-scale coupling and collective evolution dynamics problem. Thus, it is necessary to develop a statistical micro-damage model to understand its underlying mechanism. In such a model, it is essential to introduce a proper approximation at the macroscopic level, which can provide an appropriate representation for trans-scale coupling of micro-damage and continuum damage. Here, a representative volume element (RVE) was selected in the spalled region (see Fig. 9). The size of RVE is much smaller than that of a sample so that it can eliminate the influence of nonuniform stress and hydrogen concentration. In addition, there are a plenty of micro-voids in RVE.

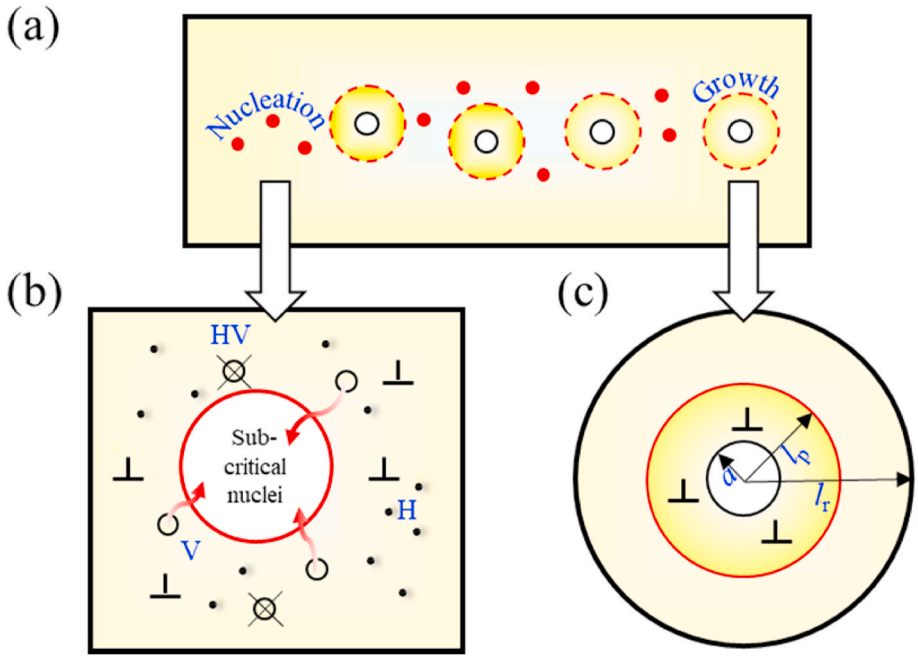

Fig. 9. Schematic of the hydrogen-retarded damage model in (a) RVE with (b) nucleation and (c) growth of micro-voids.

5.1. Theoretical framework

There are four main types of multi-scale coupling during the damage evolution of RVE in hydrogen-rich environment: hydrogen and various micro-defects such as vacancies and dislocations; individual micro-voids at a mesoscopic level; a continuum damage field and the mesoscopic evolution of micro-voids; and damage and stress fields at a macroscopic level. Thus, the evolution of micro-voids serves as a bridge that connects hydrogen-induced micro-events with hydrogen-retarded macroscopic spallation. Based on the conservation law of micro-crack evolution, Bai et al. (2019, 2005, 1991) proposed a statistical micro-damage model in phase space. Similarly, by introducing the hydrogen effect on nucleation and growth of micro-voids, the evolution of micro-void number density $n(a, t)$ (Bai et al, 1991, 2005, 2019) can be represented as

$$\frac{\partial n}{\partial t}+\frac{\partial(n\dot{a})}{\partial a}=\dot{n}_{\mathrm{c}}, \tag{2}$$

where a is the radius of a micro-void, and $\dot{n}_{\mathrm{c}}$ and $\dot{a}$ are the nucleation and growth rates related to hydrogen, respectively.

When investigating the damage evolution in spallation, the mechanical behaviors of RVE should be determined. The total strain rate of RVE $\dot{\varepsilon}_{ij}$ can be represented as

$$\dot{\varepsilon}_{ij}=\dot{\varepsilon}_{\mathrm{V}}\delta_{ij}+\dot{e}_{ij}, \tag{3}$$

where $\dot{\varepsilon}_{\mathrm{V}}$ is the volumetric strain rate and $\dot{e}_{ij}$ is the deviatoric strain rate.

According to Orowan's equation, the deviatoric strain rate $\dot{e}_{ij}$ can be calculated by (Wilkerson and Ramesh, 2014)

$$\dot{e}_{ij}=\frac{\dot{s}_{ij}}{2G}+bN_{\mathrm{m}}v\frac{2s_{ij}}{3\sigma_e}<\frac{\sigma_e}{\sigma_{\mathrm{Y}}}-1>, \tag{4}$$

where s_{ij} is the deviatoric stress, G is the shear modulus, b is the magnitude of Burgers vector,$\sigma_e=\sqrt{3/2s_{ij}s_{ij}}$ is the von Mises effective stress, andσ_{Y} is the flow stress with $<>$ the Heaviside function. The dislocation velocity v is determined by the force balance equation of dislocations, and $Bv=(\sigma_e-\sigma_{\mathrm{Y}})b$, where B is the dislocation drag coefficient. At a high strain rate, the relativistic effect should be considered, and the drag coefficient is commonly expressed as $B=\frac{B_0}{1-(v/c_{\mathrm{L}})^2}$ (Austin and McDowell, 2011). Compared with the dislocation density, the dislocation velocity plays a key role in hydrogen migration (Dadfarnia et al., 2015) and micro-void growth (Wilkerson and Ramesh, 2014). Thus, the dislocation density N_{m} is set as a constant.

Combining strain hardening and strengthening effects of hydrogen (Tehranchi et al., 2017; Zhu et al., 2017), we obtain

$$\sigma_{\mathrm{Y}}=\sigma_{YH}+H\varepsilon^{\mathrm{p}}_{\mathrm{eq}}, \tag{5}$$

where $\sigma_{YH}=\sigma_{Y0}+H_{\mathrm{c}}\sqrt{\frac{Mn^0_{\mathrm{H}}}{\rho N_{\mathrm{A}}}}$ is the yield strength of an H-charged sample, σ_{Y0} is yield strength of H-free sample, H_{c} is the strengthening effect of hydrogen, M is the molar mass, n^0_{H} is the initial number of hydrogen per unit volume, and N_{A} is Avogadro's number, H is the hardening modulus, $\varepsilon^{\mathrm{p}}_{\mathrm{eq}}$ is an equivalent plastic strain.

The volumetric strain is composed of elastic and plastic parts, and the plastic volumetric strain is derived from the irreversible evolution of micro-voids (Czarnota et al., 2008), that is

$$\dot{\varepsilon}_{\mathrm{V}}=\frac{\dot{\sigma}_m}{3K}+\frac{\dot{D}}{3(1-D)}, \tag{6}$$

where σ_m is the hydrostatic stress, K is the bulk modulus, and D is the void volume fraction (or damage variable). Thus, D is determined by the ratio of voids occupying matrix (Bai et al., 1991), namely,

$$\dot{D}=\frac{4}{3}\pi\left(\int_0^\infty \dot{n}_{\mathrm{c}}a^3da+3\int_0^\infty n\dot{a}a^2da\right), \tag{7}$$

Here, the continuum damage variable represents the statistical average effect of nucleation and growth of micro-damage on the evolution of continuum damage. It serves as a trans-scale agent that connects the stress field at the macroscopic level with the evolution of micro-voids.

It is worth noting that Eq. (2–7) are composed of a closed system of equations for describing the evolution of micro-voids in HEAs under a hydrogen-rich environment. If the nucleation rate $\dot{n}_{\mathrm{c}}$ and growth rate $\dot{a}$ are known, the effect of hydrogen on micro-void nucleation, growth and spallation can be determined.

5.2. Nucleation of micro-voids

In a single-phase HEA, vacancies migrate and form vacancy clusters at the grain boundaries under external loading. Once a vacancy cluster exceeds the critical size, it may continually grow, i.e., a void is nucleated (Huang et al., 2011). The detailed lattice kinetic Monte Carlo calculations (Reina et al., 2011) demonstrated that the time-scales associated with shock compression and subsequent spall

failure were indeed long enough to permit such a mechanism and to form large vacancy cluster. Based on previous studies (Hirth and Nix, 1985; Raj and Ashby, 1975), micro-void nucleation is treated as a vacancy flowing into subcritical nuclei (Fig. 9(b)). The subcritical nuclei can be considered as situations where the mean tensile pressure σ_m is higher than the critical tensile pressure $\sigma_{nuc} = \frac{2}{3}\sigma_{Y0}\left(1 - \ln\frac{3}{2}\frac{\sigma_{Y0}}{E}\right)$ (Wilkerson and Ramesh, 2016). The nucleation rate of micro-voids is equal to the total flow of vacancies through surface of subcritical nuclei at per unit time (Curran et al., 1987; Sizmann, 1978), which can be represented as

$$\dot{n}_c(a) = 4\pi a^2 J_{va} n_{nuc}(a) < \frac{\sigma_m}{\sigma_{nuc}} - 1 >, \tag{8}$$

where D_{va} is the diffusion coefficient of a vacancy, $4\pi a^2$ is the subcritical nuclei surface area, $J_{va} = D_{va}\frac{\partial n_{va}}{\partial r}|_{r=a} \approx D_{va}\frac{n_{va}}{a}$ is the vacancy diffusion flux, and $n_{nuc}(a)$ is the size distribution of the subcritical nuclei. Eq. (8) can be rewritten as:

$$\dot{n}_c(a) = 4\pi a D_{va} n_{va} n_{nuc}(a) < \frac{\sigma_m}{\sigma_{nuc}} - 1 >, \tag{9}$$

Bai et al. (2000) found that the nucleation rate $\dot{n}_c(a)$ of micro-voids can be fitted by the Weibull distribution. Hence, Eq. (9) can be rewritten as

$$\dot{n}_c(a) = 4\pi D_{va} n_{va} n_{max} \frac{a}{l_c} e^{-(a/l_c)^2} < \frac{\sigma_m}{\sigma_{nuc}} - 1 >, \tag{10}$$

where n_{max} is the maximum number of potential nucleation sites per unit volume, and l_c is the characteristic size of void nucleation.

In a hydrogen-rich environment, vacancies combine easily with hydrogen to form hydrogen-vacancy complexes owing to a high binding energy (Lu and Kaxiras, 2005; Xie et al., 2016). According to first principles calculations, hydrogen-vacancy complexes are difficult to move due to high migration energy, implying that fewer vacancies are involved in nucleation of micro-voids. Hence, it is necessary to determine the evolution of mobile hydrogen and vacancies.

During loading, the evolution of hydrogen and vacancies mainly involves the production of vacancies by plastic work and the combination of vacancies and hydrogen. Thus, a cluster dynamic model (Li et al., 2015) was employed based on the two assumptions: a vacancy only traps a hydrogen atom, and hydrogen atoms and vacancies are mobile and hydrogen-vacancy complexes are immobile. Then, the evolution rates of mobile hydrogen atoms and vacancies (Sizmann, 1978) are

$$\dot{n}_H = -4\pi r_{com}^2 J_H n_{va}, \tag{11}$$

$$\dot{n}_{va} = -4\pi r_{com}^2 J_H n_{va} + G_V, \tag{12}$$

where r_{com} is the critical combination radius, below which vacancy and hydrogen combine into complex. J_H is the hydrogen flux. According to Dadfarnia et al. (2015), hydrogen flux is divided into diffusion and dislocation transport, that is

$$J_H = J_{diff} + J_{dis},\ J_{diff} = D_H\frac{\partial n_H}{\partial x}, \tag{13}$$

where D_H is the diffusion rate of hydrogen, and n_H is the hydrogen content. Given that hydrogen atmospheres can move with dislocations, hydrogen flux induced by dislocation transport (Dadfarnia et al., 2015) can be expressed as

$$J_{dis} = \xi v n_H, \tag{14}$$

where ξ is a dimensionless constant.

Due to plastic deformation, the increasing rate of vacancies G_V (Li et al., 2015) is

$$G_V = \frac{\chi\rho N_A \Omega \sigma_e \dot{\varepsilon}}{M E_v^f}, \tag{15}$$

where χ is a dimensionless constant, Ω is the volume of atom, E_V^f is the formation energy of vacancy. So, Eqs. 11 and 12 are rewritten as:

$$\dot{n}_H = -4\pi r_{com}^2 n_{va}\left(D_H\frac{n_H}{r_{com}} + \xi v n_H\right), \tag{16}$$

$$\dot{n}_{va} = -4\pi r_{com}^2 n_{va}\left(D_H\frac{n_H}{r_{com}} + \xi v n_H\right) + \frac{\chi\rho N_A \Omega \sigma_e \dot{\varepsilon}}{M E_v^f}, \tag{17}$$

5.3. Growth of micro-voids

The growth of voids is not only related to loading conditions but also interaction between voids. At the early stage of damage evolution, the interaction between voids can be ignored owing to the large void spacing. It can be simplified as a condition in which a single void grows in a finite matrix. Early works analyzed deformation of a single void in a homogeneous rate-independent, perfectly

plastic medium (McClintock, 1964; Rice and Tracey, 1969). Based on these researches, yield criteria and flow rules were developed for porous rate-independent ductile materials (Gurson, 1977; Needleman, 1987; Tvergaard, 1982). And subsequently developed a series of single void dynamic growth theories (Johnson, 1981; Molinari and Wright, 2005; Wu et al., 2003a). Recently, several models have been proposed to consider microstructures such as grain size (Wilkerson and Ramesh, 2016) and dislocation dynamics (Wilkerson, 2017; Wilkerson and Ramesh, 2014) or free volume in metallic glasses (Huang et al, 2013, 2019). Based on TEM observations, the units of plastic deformation are dislocations and twins. Thus, a spherical void grows in spherical shell matrix with the strengthening effect of strain and strain rate (Fig. 9(c)). The spherical shell is subjected to a dynamic pressure at its boundary. Assuming that a dynamic load is identical to the remote pressure applied to RVE, the void growth governing equation (Wilkerson, 2017; Wilkerson and Ramesh, 2014) can be expressed as

$$\rho\left(1-\varphi^{1/3}\right)a\ddot{a}+\left(\frac{3}{2}-2\varphi^{1/3}+\frac{1}{2}\varphi^{4/3}\right)\rho\dot{a}^2=p-\int_a^{l_r}\frac{4\sigma_e}{r}dr, \tag{18}$$

where $\varphi=\frac{a^3}{l_r^3}$. The spatial integral, $\int_a^{l_r}\frac{4\sigma_e}{r}dr$, on the right-hand side of Eq. (18) can be decomposed into one dependent on the quasi-static flow strength R_c and the other associated with rate-sensitivity of the over-stress R_d. Here, R_c is obtained as

$$R_c=\int_a^{l_p}\frac{4\sigma_Y}{r}dr=\frac{2}{3}\sigma_{\sigma_{YH}}+\frac{2\sigma_{\sigma_{YH}}}{1+\frac{H}{E}}\ln\frac{l_p}{a}+\frac{4H}{9\left(1+\frac{H}{E}\right)}\sum_{n=1}^{\infty}\frac{1}{n^2}\left[\left(\frac{a^3-A^3}{a^3}\right)^n-\left(\frac{3\sigma_{\sigma_{YH}}}{2E}\right)^n\right], \tag{19}$$

where l_p is the plastic and elastic boundary, and A is the initial void size in an undeformed configuration. R_d can be further decomposed into viscosity, that is

$$R_d=\int_a^{l_p}\frac{4(\sigma_e-\sigma_Y)}{r}dr=\int_a^{l_p}\frac{4Bv}{rb}dr, \tag{20}$$

6. Modeling results

Based on the stress wave analysis in Fig. 1, RVE undergoes a severe compressive plastic deformation before tensile loading. As illustrated in Fig. 10, the imposed strain rate is $\dot{\varepsilon}_1=\frac{v_{shock}}{L}$, where v_{shock} is the shock velocity and L is the thickness of rear target. The peak pressure $P_{peak}=\frac{1}{1+C_L/C_0}\rho C_L v_{shock}$ and the corresponding duration is $\frac{2L_b}{C_L}$, where L_b is the distance of a spall region from rear free surface of the target. The corresponding duration of spall strength is $\frac{2L_f}{C_L}$, where L_f is the distance of a spall region from front free surface of the target.

Based on the studies on HEAs (Laplanche et al., 2016; Jiang et al., 2016), the following mechanical properties can be determined,

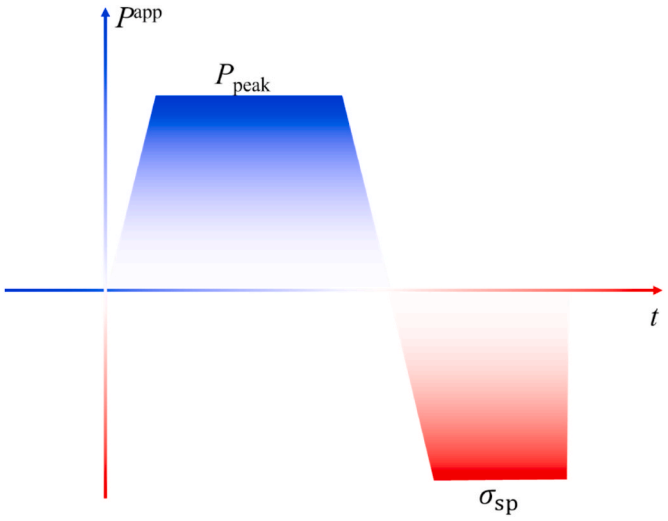

Fig. 10. The history diagram of an applied load on RVE.

such as the mass density $\rho = 7890$ kg m^{-3}, the longitudinal wave speed $C_L = 5780$ m s^{-1}, elastic constants $G = 85$ GPa and $K = 148.7$ GPa, the initial yield strength (H-free) $\sigma_{Y0} = 0.25$ GPa, the strain hardening coefficient $H = 0.85$ GPa, and the strengthening effect of hydrogen $H_c = 130$ MPa (Tehranchi et al., 2017). In the vacancy evolution, the atomic volume $\Omega = 11.8$ Å^3 and molar mass $M = 56.10$ g mol^{-1} of HEA were obtained by Vegard's law (Varvenne et al., 2016). The prepositive coefficients of diffusion about hydrogen and vacancy are 10^{-7} and 10^{-4} m^2 s^{-1}, respectively, and the critical combination radius r_{com} is approximately equal to a lattice constant of 3.56 Å (Li et al., 2012). The vacancy formation energy 1.4 eV is usually adopted (Wang et al., 2017), with Burgers vector magnitude $b = 2.55$ Å (Varvenne et al., 2016) and drag coefficient of dislocation $B_0 = 1.58\times10^{-5}$ Pa s^{-1} (Wilkerson and Ramesh, 2014). According to Wilkerson and Ramesh (2016), nucleation sites n_{max} were set as 100 μm^{-3}. However it is worth noting that there are still two unknown parameters, i.e., the characteristic size of a void nucleation distribution l_c and the dislocation density N_m, in the model. These two parameters can be estimated by fitting experimental results in an appropriate range ($l_c = 8$ nm and $N_m = 220$ μm^{-2}). The calculating algorithm for the evolution of stress, hydrogen, vacancies and voids is given in Appendix C.

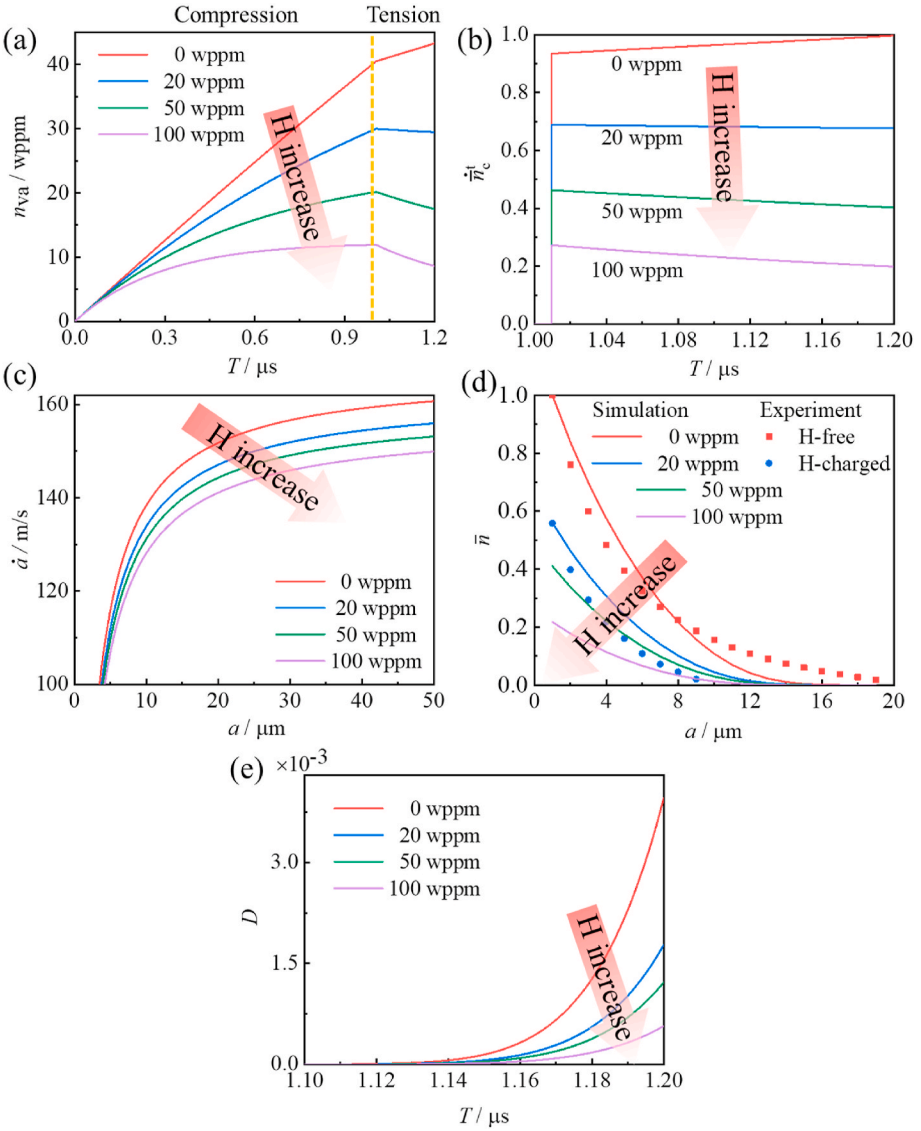

Fig. 11. Evolution of (a) vacancy and (b) the micro-void nucleation rate, (c) the growth rate as a function of void size, (d) the cumulative void number density distribution, and (e) the damage evolution under different initial hydrogen contents, where (b) and (d) are normalized by their maximum values.

6.1. Influence of hydrogen

The nucleation rate of micro-voids in Eq. (10) can be decomposed into a size-dependent part $\frac{a}{l_c}e^{-(a/l_c)^2}$, and a time-dependent part, $n_c^t = 4\pi D_{va} n_{va} n_{\max} < \frac{\sigma_m}{\sigma_{nuc}} - 1 >$, where n_c^t is proportional to the vacancy content. As shown in Fig. 11(a), the mobile vacancy content decreases with the increase of initial hydrogen concentration due to formation of immobile hydrogen-vacancy complexes. As shown in Fig. 11(b), when the mean stress is larger than σ_{nuc} in an H-free sample, the nucleation rate increases, rapidly at first and then gradually increases with time. As the increase of initial hydrogen concentration, the rising amplitude decreases and the following evolution varies from increasing to decreasing with time, which is consistent with the evolution of vacancies in tensile region. That is, stress and migration of vacancies dominate the void nucleation. Hydrogen pinning vacancies leads to reduction of the vacancy content involved in a nucleation process. Simultaneously, hydrogen increases the critical stress of nucleation, which decreases the nucleation rate.

The resistance of micro-void growth in Eq. (18) includes static and dynamic resistance caused by dislocation motion. In calculations, the imposed load of 2.13 GPa (i.e., the impact velocity of 500 m s^{-1}) is larger than the critical static resistance ($4\sigma_{Y0}$), which belongs to a supercritical stress state (Wu et al., 2003b). In this state, a micro-void growth process undergoes two stages (Wilkerson and Ramesh, 2014). One is a rapidly increasing stage dominated by dislocation motion with a growth rate being proportional to radius $\dot{a} = \frac{1}{3}abN_m C_L$, and the other is governed by micro-inertia with a growth rate of $\dot{a} = \sqrt{\frac{2(P-R_c)}{3\rho}}$, where R_c is the static resistance. When hydrogen is introduced into HEA, it results in increase of the local strength (Fig. 5). According to Eqs. (5) and (19), R_c is proportional to the material strength. Thus, hydrogen increases the growth resistance of micro-voids, which leads to decrease of the growth rate of micro-voids (Fig. 11(c)).

Hydrogen reducing nucleation and growth rates of voids leads to decrease of the number density of micro-voids (Fig. 11(d)). Furthermore, a three-dimensional void size distribution was obtained by transformation from the two-dimensional void size distribution (see Fig. 4) (Bai et al., 1993), which is in good agreement with experimental results. As shown in Fig. 11(e), damage exponentially increases due to the decrease of deformation resistance, but obviously decreases with the increase of hydrogen. That is, hydrogen can effectively hinder spallation damage. Hence, in the same impact velocity, although there are almost the same spall strengths of H-free and H-charged samples, damage is significantly hindered due to the decrease of inherent nucleation and growth rates of micro-voids in hydrogen environments.

6.2. Influence of impact velocity

With the increase of impact velocity, the imposed strain rate and applied stress increase and thus, vacancies producing by plastic work both increase by ~10% in H-free and H-charged HEAs (Fig. 12(a)). The nucleation rate of voids is consistent with the vacancy evolution in tensile section (Fig. 12(b)). In the early stage of void growth, dislocations emitted from micro-voids can move with the subsonic velocity owing to the high strain rate around micro-voids, $\dot{a}/a \sim 10^8$ s^{-1} (Bringa et al., 2010; Tang et al., 2012). With the increase of loading rate, it is easier for dislocations around micro-voids to reach the critical velocity, which causes a higher growth rate of micro-voids. The increase in tensile stress leads to a higher growth rate dominated by an inertial effect ($\dot{a} = \sqrt{\frac{2(P-R_c)}{3\rho}}$), increasing from 160 to 240 m s^{-1} (Fig. 12(c)). Thus, the number density of voids at an impact velocity of 550 m s^{-1} is larger than that at 500 m s^{-1} in H-free and H-charged HEAs (Fig. 12(d)). This trend is consistent with experimental results (Fig. 4). Damage at 550 m s^{-1} is significant (Fig. 12(e)), which is in agreement with the results in Fig. 3.

7. Discussion

According to electron backscatter diffraction experiments, micro-voids are inclined to nucleate at grain boundaries (Fig. 6). Compared with a close-packed faced-centered cubic structure, the grain boundary is relatively loose with a weak bond energy, and atoms are more easily deformed. Meanwhile, a fast channel of vacancy movement at the grain boundary is formed easily (Hirth and Nix, 1985; Raj and Ashby, 1975), and generation and aggregation of numerous vacancies results in micro-void nucleation. From a viewpoint of thermodynamics, micro-void nucleation is a situation where work done by an applied load is greater than energy required to form the new surface area of a void and to change elastic energy (Guan et al., 2013). The grain boundary is in a high-energy state, and it is easier for atoms to pass through the nucleation barrier under external loading. Therefore, a nucleation model dominated by stress and vacancy is adopted.

As listed in Table 1, the initial vacancy content of H-charged HEA increases by 40% as compared with that of H-free HEA. Hydrogen dissolution in HEA promotes local lattice distortion and enhances atomic pressure, which pushes metal atoms out from original lattice positions and produces massive vacancies. Furthermore, Wang et al. (2017) reported that the configuration entropy effect in HEAs can significantly enhance the intrinsic vacancy concentration, that is, vacancy concentration increases with the number of elements. The vacancy content that participates in nucleation is not only related to the initial vacancy but also to interaction of defects during deformation. The atomic non-affine deformation such as diffusion of atoms, nucleation and interaction of dislocations, is always

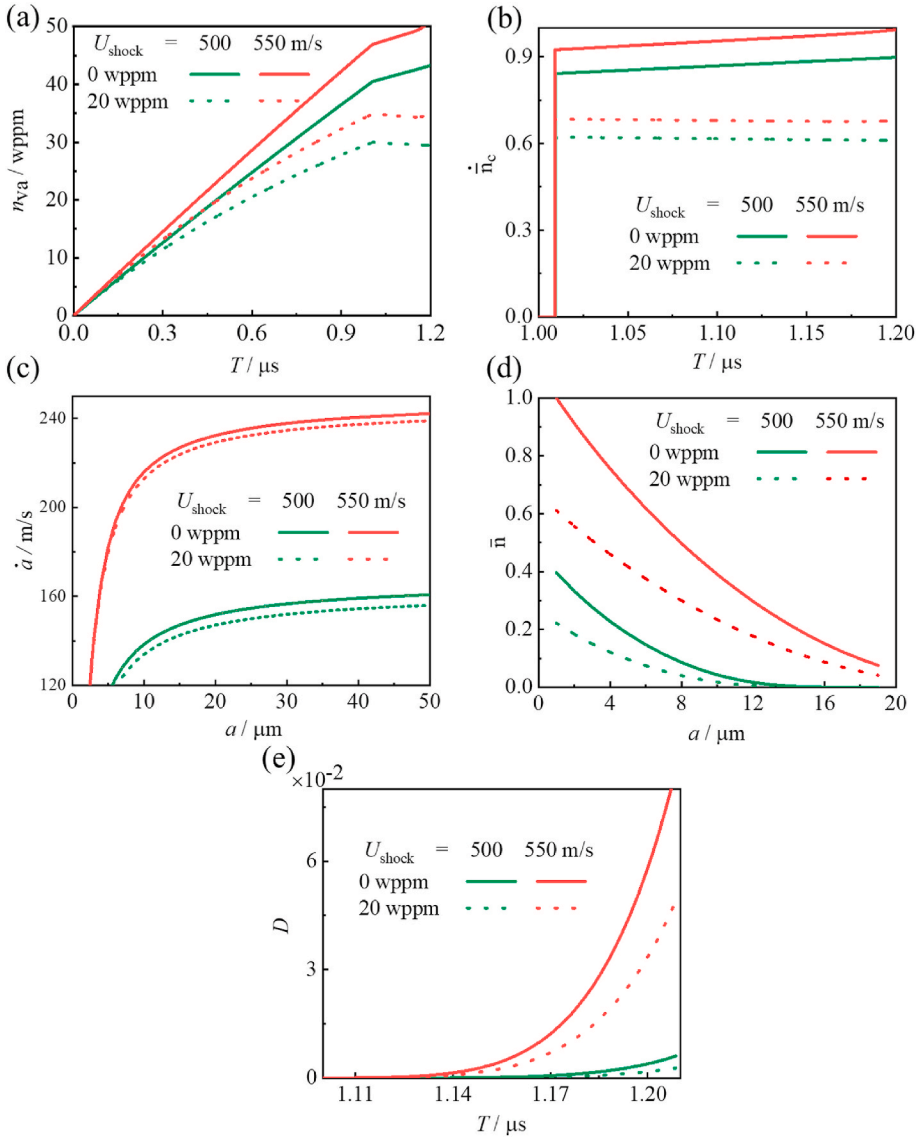

Fig. 12. Evolution of (a) vacancy and (b) the micro-void nucleation rate, (c) the growth rate as a function of void size, (d) the cumulative void number density distribution, and (e) the damage evolution under different impact velocities, where (b) and (d) are normalized by their maximum values.

accompanied by formation of new vacancies. On the other hand, vacancies are pinned by hydrogen due to formation of hydrogen-vacancy complexes with high migration energy based on first principles calculations. To quantitatively understand the effect of initial vacancy content and vacancy increment on micro-void nucleation, we established the cluster dynamic model. The vacancy generated by plastic deformation is significantly larger than the initial vacancy content, indicating that the effect of hydrogen on the initial vacancy content is negligible. Hydrogen pinning vacancies effectively reduce the number of vacancies that participate in micro-void nucleation, and simultaneously, hydrogen increases the nucleation stress, which leads to decrease of the nucleation rate.

The results of TEM in Fig. 7 show that ductile deformation microstructures of HEA are dislocations and twins. Tang et al. (2012) found that dislocations and twins nucleate at the void surface and move in matrix based on molecular dynamics, resulting in micro-void growth. This implies that the growth process of micro-voids is dominated by the ductile deformation of matrix. Wilkerson and Ramesh (2014) established a micro-void growth model by considering dislocation dynamics with the relativistic effect and obtained the growth evolution law: the rapidly increasing stage dominated by the dislocation motion,$\dot{a} = \frac{1}{3}abN_{\mathrm{m}}C_{\mathrm{L}}$ and then the micro-inertial governing stage, $\dot{a} = \sqrt{\frac{2(P-R_{\mathrm{c}})}{3\rho}}$. When hydrogen is introduced into HEA, it can effectively decrease the unstable and stable SFE of HEAs based on the first principles calculations (Xie et al., 2021), which promotes the formation of stacking faults and twins (Fig. 7). Nano-twin leads to the formation of a hierarchical twin network, where the twin boundaries act as barriers to dislocation motion (Ding et al., 2018), enhancing the local strength (Fig. 5). The strengthening effect increases the growth resistance and slows down the growth rate of micro-voids according to Eq. (19) (Fig. 11(c)).

As is well known, hydrogen in tradition alloys can be rapidly aggregated in defects by diffusion due to its light mass under external conditions. The interaction between hydrogen and defects may cause degradation of mechanical properties through enhancing localized plasticity, decohesion or formation of hydride (Robertson et al., 2015). However, hydrogen in HEAs serves as a retarder of micro-void evolution because of the following two main effects. Firstly, solid solution elements lead to a low hydrogen diffusion coefficient, which suppresses the accumulation of hydrogen. Next, the stacking fault energy of HEAs is reduced by hydrogen (Xie et al., 2021), promoting formation of nanotwins and enhancing local strain hardening that impedes the micro-damage evolution (Luo et al., 2020). In addition, hydrogen impeding the micro-void evolution has been also found in quasi-static experiments (Luo et al, 2017, 2018, 2020; Pu et al., 2018). It is shown that nano-size dimples occur in the surface region with a higher hydrogen concentration, while much coarser dimples appear in a hydrogen-poor center region. HEAs exhibit the excellent hydrogen embrittlement resistance with a little loss of ductility. Furthermore, hydrogen in spallation slowdowns the nucleation, growth and coalescence of micro-voids and enhances the dynamic damage tolerance of HEAs.

8. Conclusions

Plate impact experiments of CrMnFeCoNi with and without hydrogen were conducted to investigate the effect of hydrogen on spallation. In comparison to H-free CrMnFeCoNi, the number and size of micro-voids in H-charged samples significantly decrease, indicating that hydrogen can retard micro-void nucleation, growth and coalescence.

Based on microstructure characterization and a statistical mechanical model, the mechanism of hydrogen-retarded spallation was studied. As increase of the initial hydrogen content, the number of mobile vacancies involved in nucleation of micro-voids decreases due to formation of hydrogen-vacancy complexes with a high migration energy. That is, the nucleation rate decreases. Furthermore, the increase of local hardness and strength in H-charged HEAs enhances the resistance of void growth and decreases the growth rate. The modeling results agree with the micro-void evolution under hydrogen-rich environment.

These findings break a preconception about the deleterious effect of hydrogen. It is worth noting that more experiments are needed in order to provide a new strategy for future design and application of hydrogen-tolerant materials with superior mechanical properties.

CRediT authorship contribution statement

Zhou-Can Xie: Writing - original draft, Spallation experiment, Material characterization, First principles calculation, Multi-scale model and Writing - original draft preparation. **Chen Li:** Spallation experiment, Formal analysis. **Hai-Ying Wang:** Supervision, Writing - review & editing. **Chunsheng Lu:** Supervision, Writing - review & editing. **Lan-Hong Dai:** Supervision, Writing - review & editing.

Declaration of competing interest

The authors declare that they have no known competing financial interests or personal relationships that could have appeared to influence the work reported in this paper.

Acknowledgements

This work was supported by the National Key Research and Development Program of China (No. 2017YFB0702003), the National Natural Science Foundation of China (No. 11790292), the NSFC Basic Science Center Program for "Multiscale Problems in Nonlinear Mechanics" (No. 11988102), the Strategic Priority Research Program (No. XDB22040302 and No. XDB22040303), the Key Research Program of Frontier Sciences (No. QYZDJSSWJSC011), the Science Challenge Project (No. TZ2018001).

Appendix A. Error estimation of spall strength

In this paper, estimation of spall strength is based on measurement of the velocity pullback, $\sigma_{sp} = \frac{1}{1+C_L/C_0}\rho C_L \Delta u$, where ρ, C_L and C_0 are material properties, and Δu is determined by in the velocity history of free surface. Thus, error of spall strength is mainly originated from experimental measurements of velocity history of free surface. Here, a photonic Doppler velocimetry (PDV) system was adopted to measure the velocity of free surface. Then, the raw PDV detector data was used to calculate a power spectrum by the short time Fourier transform technique (Jensen et al., 2007). The resulting spectrogram displays the distribution of spectral power densities, encoded here by color, as a function of time and velocity (Fig. A.1), where the peak center of power spectrum (color by yellow) is taken as the measured velocity. Uncertainty in the measured velocity is the width of peak, $\Delta u_{err} = 10$ m s^{-1}, and the relative error of spall strength ($\Delta u_{err}/\ \Delta u$) is 7.9%.

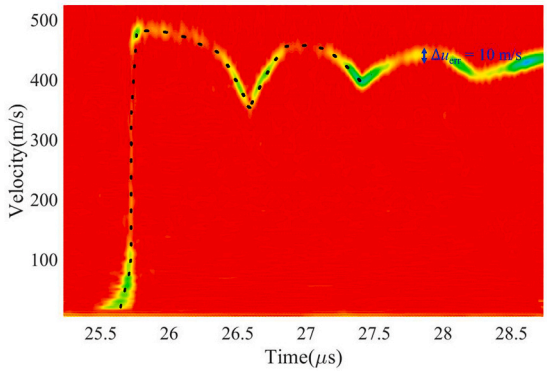

Fig. A.1. PDV power spectrum in first spallation of a sample with hydrogen

Appendix B. Spall experiments

As shown in Fig. B.1, impact velocities in the other two experiments are 480 and 500 m s^{-1}, and there are obvious spallation signals at free surface velocity profiles. The spall strengths of H-free and H-charged samples in the third experiment are 2.07 and 2.10 GPa, respectively, and they are 2.09 and 2.18 GPa in the fourth experiment.

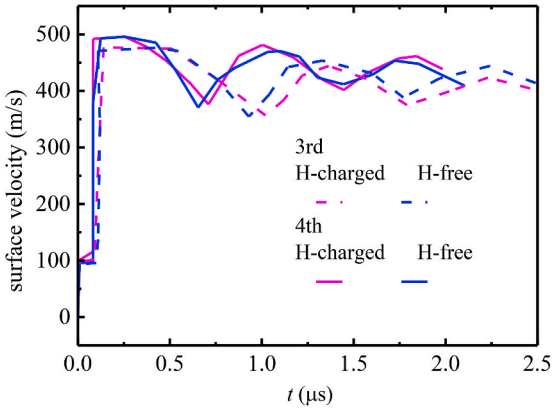

Fig. B.1. Particle-velocity profiles on free surface *versus* time in experiments.

It is seen from Fig. B. 2 that the number density of micro-voids in H-free samples is higher than that in H-charged ones, with the same trend observed for the size of micro-voids. That is, hydrogen retards nucleation and growth of micro-voids and spallation damage.

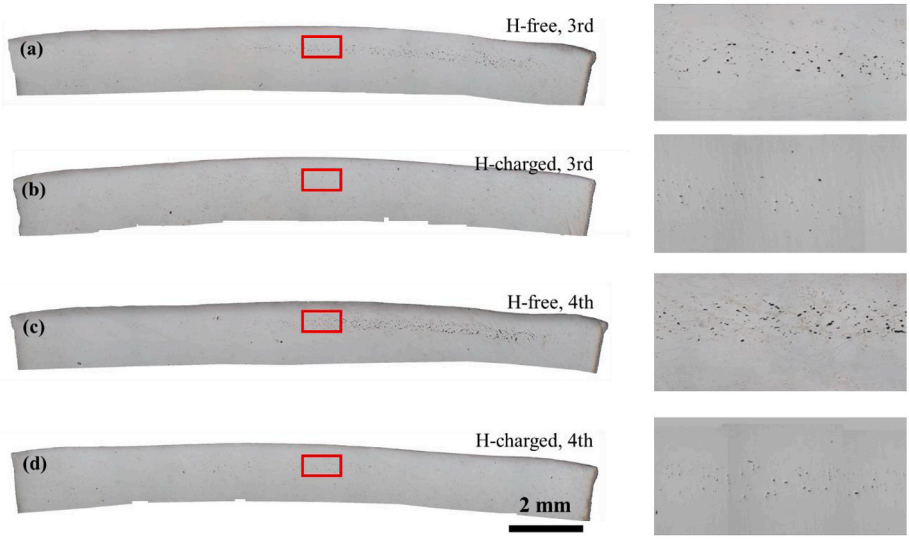

Fig. B.2. Cross sections of spalled samples observed by an optical microscope, where (a, c) and (b, d) are samples without and with hydrogen in the other two spallation experiments. Images in the right column are their corresponding magnified regions marked by red rectangles.

Appendix C. Calculation procedure

A time increment method was applied to explore the micro-void evolution under uniaxial strain with the following main steps:

(1) Set initial hydrogen and vacancy concentrations to be the measured values, and the other variables as zero.
(2) Given time and pressure increments (see Fig. 10), update stress and strain by using Eq. (3−6) and vacancy and hydrogen concentrations by Eqs. (16) and (17).
(3) If $\sigma_m > \sigma_{\text{nuc}}$, update the nucleation rate of micro-voids (Eq. (10)) and the growth rate (Eq. (18)), as well as the void number density and damage (Eq. (2) and (7)); otherwise, skip to the next step.
(4) Repeat steps (2) and (3) till the imposed time.

Provided that a void growth process is precisely taken into account (Eq. (18)), the current state and history of individual voids should be recorded in each increment step. This would consume a huge amount of calculation resources. Thus, to obtain a relationship between the growth rate and void size, a single void growth process was calculated under $P = 2.13$ GPa.

As shown in Fig. C.1, the void growth rate linearly increases to a stable value. A similar tendency was observed in the void growth with a higher strain rate ($\dot{\varepsilon} > 10^6$ s^{-1}) (Wilkerson, 2014). Here, it is worth noting that the strain rate around a micro-void ($\dot{\varepsilon} \sim \dot{a}/a$) is much higher ($\dot{\varepsilon} >> 10^6$ s^{-1}) than the imposed strain rate of 10^4 s^{-1}. Under the same loading level, the linear growth rate and final stable value of a void are independent of its initial size. Based on experimental observations, micro-void nucleation originates from a vacancy cluster, with a size on the order of nanometers. Hence, the initial void size was assumed to be 10 nm with an initial velocity of zero.

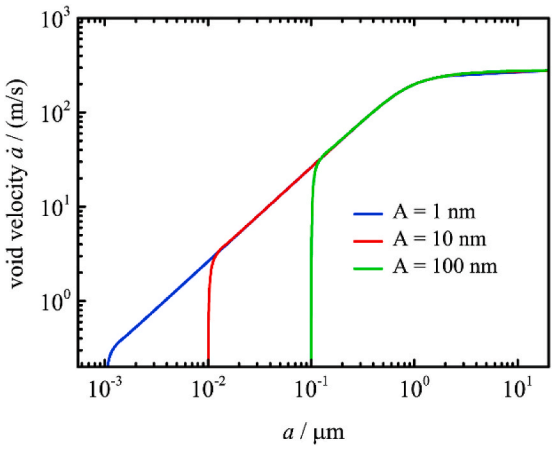

Fig. C.1. The growth rate of a micro-void with different initial radii as a function of its size.

References

Abdolvand, H., 2019. Progressive modelling and experimentation of hydrogen diffusion and precipitation in anisotropic polycrystals. Int. J. Plast. 116, 39–61.

Austin, R.A., McDowell, D.L., 2011. A dislocation-based constitutive model for viscoplastic deformation of fcc metals at very high strain rates. Int. J. Plast. 27, 1–24.

Bai, Y., Xia, M., Ke, F., Guo, W., Ling, Z., 1993. Statistical interpretation on the relationship between the volumetric and sectional size distributions of disordered meso-structures. Acta Phys. Sin. 42, 351–359.

Bai, Y.L., Bai, J., Li, H.L., Ke, F.J., Xia, M.F., 2000. Damage evolution, localization and failure of solids subjected to impact loading. Int. J. Impact Eng. 24, 685–701.

Bai, Y.L., Fujiu, K., Mengfen, X., 1991. Formulation of statistical evolution of microcracks in solids. Acta Mech. Sin. 7, 59–66.

Bai, Y.L., Wang, H.Y., Xia, M.F., Ke, F.J., 2005. Statistical mesomechanics of solid, linking coupled multiple space and time scales. Appl. Mech. Rev. 58, 372–388.

Bai, Y.L., Xia, M., Ke, F., 2019. Statistical Meso-Mechanics of Damage and Failure: How Microdamage Induces Disaster. Springer, Singapore.

Barrera, O., Bombac, D., Chen, Y., Daff, T.D., Galindo-Nava, E., Gong, P., Haley, D., Horton, R., Katzarov, I., Kermode, J.R., Liverani, C., Stopher, M., Sweeney, F., 2018. Understanding and mitigating hydrogen embrittlement of steels: a review of experimental, modelling and design progress from atomistic to continuum. J. Mater. Sci. 53, 6251–6290.

Bringa, E.M., Traiviratana, S., Meyers, M.A., 2010. Void initiation in fcc metals: effect of loading orientation and nanocrystalline effects. Acta Mater. 58, 4458–4477.

Cantor, B., Chang, I.T.H., Knight, P., Vincent, A.J.B., 2004. Microstructural development in equiatomic multicomponent alloys. Mater. Sci. Eng., A 375, 213–218.

Castelluccio, G.M., Geller, C.B., McDowell, D.L., 2018. A rationale for modeling hydrogen effects on plastic deformation across scales in FCC metals. Int. J. Plast. 111, 72–84.

Curran, D.R., Seaman, L., Shockey, D.A., 1987. Dynamic failure of solids. Phys. Rep. 147, 253–388.

Czarnota, C., Jacques, N., Mercier, S., Molinari, A., 2008. Modelling of dynamic ductile fracture and application to the simulation of plate impact tests on tantalum. J. Mech. Phys. Solid. 56, 1624–1650.

Dadfarnia, M., Martin, M.L., Nagao, A., Sofronis, P., Robertson, I.M., 2015. Modeling hydrogen transport by dislocations. J. Mech. Phys. Solid. 78, 511–525.

Di Leo, C.V., Anand, L., 2013. Hydrogen in metals: a coupled theory for species diffusion and large elastic-plastic deformations. Int. J. Plast. 43, 42–69.

Ding, J., Yu, Q., Asta, M., Ritchie, R.O., 2018. Tunable stacking fault energies by tailoring local chemical order in CrCoNi medium-entropy alloys. Proc. Natl. Acad. Sci. Unit. States Am. 115, 8919–8924.

Dlubek, G., Brümmer, O., Hensel, E., 1976. Positron annihilation investigation for an estimation of the dislocation density and vacancy concentration of plastically deformed polycrystalline Ni of different purity. Phys. Status Solidi 34, 737–746.

Fang, Q., Chen, Y., Li, J., Jiang, C., Liu, B., Liu, Y., Liaw, P.K., 2019. Probing the phase transformation and dislocation evolution in dual-phase high-entropy alloys. Int. J. Plast. 114, 161–173.

George, E.P., Raabe, D., Ritchie, R.O., 2019. High-entropy alloys. Nat. Rev. Mater. 4, 515–534.

Gludovatz, B., Hohenwarter, A., Catoor, D., Chang, E.H., George, E.P., Ritchie, R.O., 2014. A fracture-resistant high-entropy alloy for cryogenic applications. Science 345, 1153–1158.

Guan, P., Lu, S., Spector, M.J.B., Valavala, P.K., Falk, M.L., 2013. Cavitation in amorphous solids. Phys. Rev. Lett. 110, 185502.

Gurson, A.L., 1977. Continuum theory of ductile rupture by void nucleation and growth: Part 1 - yield criteria and flow rules for porous ductile media. J. Eng. Mater. Technol. Trans. ASME 99, 2–15.

Hasan, M.N., Liu, Y.F., An, X.H., Gu, J., Song, M., Cao, Y., Li, Y.S., Zhu, Y.T., Liao, X.Z., 2019. Simultaneously enhancing strength and ductility of a high-entropy alloy via gradient hierarchical microstructures. Int. J. Plast. 123, 178–195.

Hirth, J.P., Nix, W.D., 1985. Analysis of cavity nucleation in solids subjected to external and internal stresses. Acta Metall. 33, 359–368.

Hopkinson, B., 1914. X. A method of measuring the pressure produced in the detonation of high, explosives or by the impact of bullets. Philos. Trans. R. Soc. Lond. - Ser. A Contain. Pap. a Math. or Phys. Character 213, 437–456.

Huang, X., Ling, Z., Dai, L.H., 2019. Influence of surface energy and thermal effects on cavitation instabilities in metallic glasses. Mech. Mater. 131, 113–120.

Huang, X., Ling, Z., Dai, L.H., 2013. Cavitation instabilities in bulk metallic glasses. Int. J. Solid Struct. 50, 1364–1372.

Huang, X., Ling, Z., Zhang, H.S., Ma, J., Dai, L.H., 2011. How does spallation microdamage nucleate in bulk amorphous alloys under shock loading? J. Appl. Phys. 11, 103519.

Jensen, B.J., Holtkamp, D.B., Rigg, P.A., Dolan, D.H., 2007. Accuracy limits and window corrections for photon Doppler velocimetry. J. Appl. Phys. 101, 013523.

Jiang, Z.J., He, J.Y., Wang, H.Y., Zhang, H.S., Lu, Z.P., Dai, L.H., 2016. Shock compression response of high entropy alloys. Mater. Res. Lett. 4, 226–232.

Johnson, J.N., 1981. Dynamic fracture and spallation in ductile solids. J. Appl. Phys. 52, 2812–2825.

Johnson, W.H., 1875. On some remarkable changes produced in iron and steel by the action of hydrogen and acids. Proc. Roy. Soc. Lond. 23, 168–179.

Kanel', G.I., Zaretsky, E.B., Razorenov, S.V., Ashitkov, S.I., Fortov, V.E., 2017. Unusual plasticity and strength of metals at ultra-short load durations. Phys. Usp. 60, 490–508.

Kansy, J., 1996. Microcomputer program for analysis of positron annihilation lifetime spectra. Nucl. Instruments Methods Phys. Res. Sect. A Accel. Spectrometers, Detect. Assoc. Equip. 374, 235–244.

Kresse, G., Furthmüller, J., 1996. Efficiency of ab-initio total energy calculations for metals and semiconductors using a plane-wave basis set. Comput. Mater. Sci. 6, 15–50.

Ku, A.Y., Khan, A.S., Gnaupel-Herold, T., 2020. Quasi-static and dynamic response, and texture evolution of two overaged Al 7056 alloy plates in T761 and T721 tempers: experiments and modeling. Int. J. Plast. 130, 102679.

Laplanche, G., Kostka, A., Horst, O.M., Eggeler, G., George, E.P., 2016. Microstructure evolution and critical stress for twinning in the CrMnFeCoNi high-entropy alloy. Acta Mater. 118, 152–163.

Li, Q.J., Sheng, H., Ma, E., 2019a. Strengthening in multi-principal element alloys with local-chemical-order roughened dislocation pathways. Nat. Commun. 10, 3563.

Li, S., Li, Y., Lo, Y.C., Neeraj, T., Srinivasan, R., Ding, X., Sun, J., Qi, L., Gumbsch, P., Li, J., 2015. The interaction of dislocations and hydrogen-vacancy complexes and its importance for deformation-induced proto nano-voids formation in α-Fe. Int. J. Plast. 74, 175–191.

Li, W., Chen, S., Liaw, P.K., 2020a. Discovery and design of fatigue-resistant high-entropy alloys. Scripta Mater. 187, 68–75.

Li, Y., Li, W., Min, N., Liu, H., Jin, X., 2020b. Homogeneous elasto-plastic deformation and improved strain compatibility between austenite and ferrite in a co-precipitation hardened medium Mn steel with enhanced hydrogen embrittlement resistance. Int. J. Plast. 133, 102805.

Li, Y.G., Zhou, W.H., Huang, L.F., Zeng, Z., Ju, X., 2012. Cluster dynamics modeling of accumulation and diffusion of helium in neutron irradiated tungsten. J. Nucl. Mater. 431, 26–32.

Li, Z., Zhao, S., Alotaibi, S.M., Liu, Y., Wang, B., Meyers, M.A., 2018. Adiabatic shear localization in the CrMnFeCoNi high-entropy alloy. Acta Mater. 151, 424–431.

Li, Z., Zhao, S., Ritchie, R.O., Meyers, M.A., 2019b. Mechanical properties of high-entropy alloys with emphasis on face-centered cubic alloys. Prog. Mater. Sci. 102, 296–345.

Lieou, C.K.C., Mourad, H.M., Bronkhorst, C.A., 2019. Strain localization and dynamic recrystallization in polycrystalline metals: thermodynamic theory and simulation framework. Int. J. Plast. 119, 171–187.

Lu, G., Kaxiras, E., 2005. Hydrogen embrittlement of aluminum: the crucial role of vacancies. Phys. Rev. Lett. 94, 155501.

Luo, H., Li, Z., Raabe, D., 2017. Hydrogen enhances strength and ductility of an equiatomic high-entropy alloy. Sci. Rep. 7, 1–7.

Luo, H., Lu, W., Fang, X., Ponge, D., Li, Z., Raabe, D., 2018. Beating hydrogen with its own weapon: nano-twin gradients enhance embrittlement resistance of a high-entropy alloy. Mater. Today 21, 1003–1009.

Luo, H., Sohn, S.S., Lu, W., Li, L., Li, X., Soundararajan, C.K., Krieger, W., Li, Z., Raabe, D., 2020. A strong and ductile medium-entropy alloy resists hydrogen embrittlement and corrosion. Nat. Commun. 11, 3081.

Mayer, A.E., Mayer, P.N., 2020. Strain rate dependence of spall strength for solid and molten lead and tin. Int. J. Fract. 222, 171–195.

McClintock, F.A., 1964. A criterion for ductile fracture by the growth of holes. J. Appl. Mech. Trans. ASME 35, 363–371.

Meyers, M.A., Aimone, C.T., 1983. Dynamic fracture (spalling) of metals. Prog. Mater. Sci. 28, 1–96.
Ming, K., Li, L., Li, Z., Bi, X., Wang, J., 2019. Grain boundary decohesion by nanoclustering Ni and Cr separately in CrMnFeCoNi high-entropy alloys. Sci. Adv. 5, 0639.
Molinari, A., Wright, T.W., 2005. A physical model for nucleation and early growth of voids in ductile materials under dynamic loading. J. Mech. Phys. Solid. 53, 1476–1504.
Murty, B.S., Yeh, J.W., Ranganathan, S., Bhattacharjee, P.P., 2019. High-entropy Alloys. Elsevier.
Nagumo, M., 2007. Mechanism of hydrogen-related failure II. Corros. Eng. 56, 491–518.
Nagumo, M., 2001. Function of hydrogen in embrittlement of high-strength steels. ISIJ Int. 41, 590–598.
Needleman, A., 1987. A continuum model for void nucleation by inclusion debonding. J. Appl. Mech. Trans. ASME 54, 525–531.
Oliver, W.C., Pharr, G.M., 1992. An improved technique for determining hardness and elastic modulus using load and displacement sensing indentation experiments. J. Mater. Res. 7, 1564–1583.
Oriani, R.A., 1972. A mechanistic theory of hydrogen embrittlement of steels. Ber. Bunsen Ges. Phys. Chem. 76, 848–857.
Pu, Z., Chen, Y., Dai, L.H., 2018. Strong resistance to hydrogen embrittlement of high-entropy alloy. Mater. Sci. Eng., A 736, 156–166.
Raj, R., Ashby, M.F., 1975. Intergranular fracture at elevated temperature. Acta Metall. 23, 653–666.
Reina, C., Marian, J., Ortiz, M., 2011. Nanovoid nucleation by vacancy aggregation and vacancy-cluster coarsening in high-purity metallic single crystals. Phys. Rev. B 84, 104117.
Remington, T.P., Hahn, E.N., Zhao, S., Flanagan, R., Mertens, J.C.E., Sabbaghianrad, S., Langdon, T.G., Wehrenberg, C.E., Maddox, B.R., Swift, D.C., Remington, B.A., Chawla, N., Meyers, M.A., 2018. Spall strength dependence on grain size and strain rate in tantalum. Acta Mater. 158, 313–329.
Rice, J.R., Tracey, D.M., 1969. On the ductile enlargement of voids in triaxial stress fields. J. Mech. Phys. Solid. 17, 201–217.
Rittel, D., Landau, P., Venkert, A., 2008. Dynamic recrystallization as a potential cause for adiabatic shear failure. Phys. Rev. Lett. 101, 165501.
Robertson, I.M., Birnbaum, H.K., 1986. An HVEM study of hydrogen effects on the deformation and fracture of nickel. Acta Metall. 34, 353–366.
Robertson, I.M., Sofronis, P., Nagao, A., Martin, M.L., Wang, S., Gross, D.W., Nygren, K.E., 2015. Hydrogen embrittlement understood. Metall. Mater. Trans. A Phys. Metall. Mater. Sci. 46, 2323–2341.
Sheppard, D., Xiao, P., Chemelewski, W., Johnson, D.D., Henkelman, G., 2012. A generalized solid-state nudged elastic band method. J. Chem. Phys. 136, 074103.
Shi, P., Ren, W., Zheng, T., Ren, Z., Hou, X., Peng, J., Hu, P., Gao, Y., Zhong, Y., Liaw, P.K., 2019. Enhanced strength–ductility synergy in ultrafine-grained eutectic high-entropy alloys by inheriting microstructural lamellae. Nat. Commun. 10, 489.
Sizmann, R., 1978. The effect of radiation upon diffusion in metals. J. Nucl. Mater. 69–70, 386–412.
Strand, O.T., Goosman, D.R., Martinez, C., Whitworth, T.L., Kuhlow, W.W., 2006. Compact system for high-speed velocimetry using heterodyne techniques. Rev. Sci. Instrum. 77, 83108.
Tabata, T., Birnbaum, H.K., 1983. Direct observations of the effect of hydrogen on the behavior of dislocations in iron. Scripta Metall. 17, 947–950.
Tang, Y., Bringa, E.M., Meyers, M.A., 2012. Ductile tensile failure in metals through initiation and growth of nanosized voids. Acta Mater. 60, 4856–4865.
Tehranchi, A., Yin, B., Curtin, W.A., 2017. Softening and hardening of yield stress by hydrogen–solute interactions. Philos. Mag. 97, 400–418.
Thomas, S.L., Srikanth, P., 2020. Vacancy diffusion in multi-principal element alloys: the role of chemical disorder in the ordered lattice. Acta Mater. 196, 144–153.
Thurston, K.V.S., Gludovatz, B., Hohenwarter, A., Laplanche, G., George, E.P., Ritchie, R.O., 2017. Effect of temperature on the fatigue-crack growth behavior of the high-entropy alloy CrMnFeCoNi. Intermetallics 88, 65–72.
Tvergaard, V., 1982. On localization in ductile materials containing spherical voids. Int. J. Fract. 18, 237–252.
Varvenne, C., Luque, A., Curtin, W.A., 2016. Theory of strengthening in fcc high entropy alloys. Acta Mater. 118, 164–176.
Wan, L., Geng, W.T., Ishii, A., Du, J.P., Mei, Q., Ishikawa, N., Kimizuka, H., Ogata, S., 2019. Hydrogen embrittlement controlled by reaction of dislocation with grain boundary in alpha-iron. Int. J. Plast. 112, 206–219.
Wang, Z., Liu, C.T., Dou, P., 2017. Thermodynamics of vacancies and clusters in high-entropy alloys. Phys. Rev. Mater. 1, 43601.
Wang, Z., Wang, C., Zhao, Y.L., Hsu, Y.C., Li, C.L., Kai, J.J., Liu, C.T., Hsueh, C.H., 2020. High hardness and fatigue resistance of CoCrFeMnNi high entropy alloy films with ultrahigh-density nanotwins. Int. J. Plast. 102726.
Wilkerson, J.W., 2017. On the micromechanics of void dynamics at extreme rates. Int. J. Plast. 95, 21–42.
Wilkerson, J.W., Ramesh, K.T., 2016. Unraveling the anomalous grain size dependence of cavitation. Phys. Rev. Lett. 117, 215503.
Wilkerson, J.W., Ramesh, K.T., 2014. A dynamic void growth model governed by dislocation kinetics. J. Mech. Phys. Solid. 70, 262–280.
Wu, X.Y., Ramesh, K.T., Wright, T.W., 2003a. The coupled effects of plastic strain gradient and thermal softening on the dynamic growth of voids. Int. J. Solid Struct. 40, 6633–6651.
Wu, X.Y., Ramesh, K.T., Wright, T.W., 2003b. The dynamic growth of a single void in a viscoplastic material under transient hydrostatic loading. J. Mech. Phys. Solid. 51, 1–26.
Xie, D., Li, S., Li, M., Wang, Z., Gumbsch, P., Sun, J., Ma, E., Li, J., Shan, Z., 2016. Hydrogenated vacancies lock dislocations in aluminium. Nat. Commun. 7, 1–7.
Xie, Z., Wang, Y., Lu, C., Dai, L., 2021. Sluggish hydrogen diffusion and hydrogen decreasing stacking fault energy in a high-entropy alloy. Mater. Today Commun. 26, 101902.
Xiong, J., Zhu, Y., Li, Z., Huang, M., 2018. Hydrogen-enhanced interfacial damage in Ni-based single crystal superalloy. Scripta Mater. 143, 30–34.
Yeh, J.W., Chen, S.K., Lin, S.J., Gan, J.Y., Chin, T.S., Shun, T.T., Tsau, C.H., Chang, S.Y., 2004. Nanostructured high-entropy alloys with multiple principal elements: novel alloy design concepts and outcomes. Adv. Eng. Mater. 6, 299–303.
Yuan, S., Zhu, Y., Huang, M., Liang, S., Li, Z., 2020. Dislocation-density based crystal plasticity model with hydrogen-enhanced localized plasticity in polycrystalline face-centered cubic metals. Mech. Mater. 148, 103472.
Zhang, F.X., Zhao, S., Jin, K., Xue, H., Velisa, G., Bei, H., Huang, R., Ko, J.Y.P., Pagan, D.C., Neuefeind, J.C., Weber, W.J., Zhang, Y., 2017. Local structure and short-range order in a NiCoCr solid solution alloy. Phys. Rev. Lett. 118, 205501.
Zhang, T.W., Ma, S.G., Zhao, D., Wu, Y.C., Zhang, Y., Wang, Z.H., Qiao, J.W., 2020. Simultaneous enhancement of strength and ductility in a NiCoCrFe high-entropy alloy upon dynamic tension: micromechanism and constitutive modeling. Int. J. Plast. 124, 226–246.
Zhao, Y., Lee, D.H., Seok, M.Y., Lee, J.A., Phaniraj, M.P., Suh, J.-Y., Ha, H.-Y., Kim, J.Y., Ramamurty, U., Jang, J., 2017a. Resistance of CoCrFeMnNi high-entropy alloy to gaseous hydrogen embrittlement. Scripta Mater. 135, 54–58.
Zhao, Y., Lee, D.H., Kim, W.J., Seok, M.Y., Kim, J.Y., Han, H.N., Suh, J.Y., Ramamurty, U., Jang, J. il, 2018. Influence of pre-strain on the gaseous hydrogen embrittlement resistance of a high-entropy alloy. Mater. Sci. Eng., A 718, 43–47.
Zhao, Y., Lee, D.H., Lee, J.A., Kim, W.J., Han, H.N., Ramamurty, U., Suh, J.Y., Jang, J., 2017b. Hydrogen-induced nanohardness variations in a CoCrFeMnNi high-entropy alloy. Int. J. Hydrogen Energy 42, 12015–12021.
Zhu, Y., Li, Z., Huang, M., Fan, H., 2017. Study on interactions of an edge dislocation with vacancy-H complex by atomistic modelling. Int. J. Plast. 92, 31–44.
Zunger, A., Wei, S.H., Ferreira, L.G., Bernard, J.E., 1990. Special quasirandom structures. Phys. Rev. Lett. 65, 353.